This is an Accepted Manuscript of an article published by Taylor & Francis in Journal of Spatial Science on 11 Mar 2020 (published online), available at: http://www.tandfonline.com/10.1080/14498596.2020.1734109.

Integrity Monitoring Using Multi-GNSS Pseudorange Observations in the Urban Environment Combining ARAIM and 3D City Models

Ahmed El-Mowafy, Bing Xu, and Li-Ta Hsu

February 10, 2020

Abstract

Integrity is a key positioning performance parameter in navigation. A novel approach is proposed for integrity monitoring that combines the Advanced Receiver Autonomous Integrity Monitoring (ARAIM) with Non Line-of-Sight (NLOS) detection method using 3D city models to aid multi-constellation GNSS positioning in challenging urban scenarios. The former method estimates the Protection Levels associated with the satellite geometry, detects and excludes unreliable observations, and the latter method helps in detecting and excluding NLOS and identifying multipath signals. A demonstration of the proposed approach is performed with real data in a dense urban area in Hong Kong. The combined technique is tested via Single Point Positioning and simulated DGNSS positioning using a commercial grade receiver. An improvement of fault detection capability and accordingly the obtained accuracy is shown when combining the two methods, NLOS detection and ARAIM, compared to applying each method individually.

Keywords: Integrity Monitoring, ARAIM, 3D City Models, Multi-GNSS, NLOS

1 Introduction

Integrity is a key performance parameter in navigation. Integrity is about the trust that a user can have in the indicated position information, and strictly relates to the system capability to detect and identify possible anomalies corrupting the navigation solution. Integrity monitoring can be performed at the user level exploiting the redundancy of the observations available. In this work, we apply the Advanced Receiver Autonomous Integrity Monitoring (ARAIM) approach (Blanch et al. 2007), which relies on a Multiple Hypothesis model and a Solution Separation test-based fault detection algorithm. Furthermore, we make use of a 3D city model to predict satellites visibility at the user, and determine the occurrence of NLOS or multipath in real time. The combined use of the ARAIM algorithm and 3D maps improves reliable determination of which observations are to be trusted, and which observations can be excluded or de-weighted.

The concept of RAIM was developed to safeguard the navigation integrity by means of self-contained fault detection at the GNSS navigation receiver. Fault detection, a fundamental task in RAIM, usually

relies on statistical hypothesis testing, under the assumption that the observation errors in the fault-free mode are normally distributed with zero mean. One may test the validity of this assumed hypothesis by means of a Chi-square distributed sum-of-squared-residuals (Walter & Enge 1995). Depending on the parametrization of the underlying model, many implementations of these test-statistics exist (Blanch et al. 2015, El-Mowafy & Kubo 2017, Joerger & Pervan 2016). In addition to application in the observations domain, integrity monitoring can be implemented in the position domain, which is applied in this paper, following the ARAIM Multiple Hypothesis Solution Separation (MHSS) method proposed in (Blanch et al. 2015). The trust in the position solution is evaluated by the Protection Levels (PLs), which are defined as the maximum errors that can possibly occur with probability larger than the allowed Probability of Hazardous Misleading Information (P_{HMI}), without an Alert being timely raised (Parkinson & Axelrad 1988). ARAIM requires observing enough number of satellites to enable positioning with some redundancy. Nowadays, this is possible in large sections in the urban environment due to the presence of multiple GNSS constellations.

While the RAIM algorithm can guarantee protection against occasional outliers, occurring anomalies or faults, it is not specifically designed to cope with frequent recurring biases or errors, as for instance multipath and NLOS. In urban environments, GNSS positioning performance is heavily degraded by the presence of high-rise buildings, which block, reflect and diffract the signals, causing multipath and NLOS. In fact, buildings and other obstacles degrade positioning in three ways: 1) signals may be completely blocked, and are unavailable for positioning, 2) direct signals are blocked, but the signals are still received via a reflected path, with the NLOS reception, 3) both direct Line-Of-Sight (LOS) and reflected signals are received, causing multipath interference. Code signals can thus exhibit positive ranging errors of tens of meters in dense urban areas. It is therefore important to develop a positioning method resistant against NLOS and multipath, and that does not rely only on a standard RAIM technique.

For positioning by GNSS in vehicle navigation, 3D-map aiding and 3D city models of the buildings can be used to predict the NLOS signals and eliminate them from the position solution (Bourdeau & Sahmoudi 2012, Hsu et al. 2015). Different approaches have been proposed in the literature that define search areas centered on the conventional GNSS position solution and attribute weights to hypotheses of NLOS or LOS signal. Unless the search area is small, these approaches are very computationally intensive as the path delay cannot easily be pre-computed (Adjrad & Groves 2016, Suzuki 2016).

In Section 2, we describe the proposed ARAIM approach used, first defining a model for the possible faults occurring, and then introducing the PLs computation method derived from ARAIM. In Section 3, we describe the 3D model-based method to determine the satellite visibility at each location on the route. In Section 4, test results are given for static and kinematic tests in an urban area in Hong Kong. Conclusions and recommendations are gathered in Section 6.

2 Proposed ARAIM

This section discusses the proposed RAIM method for land navigation.

2.1 Outliers/Faults model

In the fault-free state, the GNSS observation equation can be expressed as:

$$\mathcal{H}_o: \quad y = Ax + e \tag{1}$$

where y is the vector of observables, computed as the difference between the observations and their estimated values from the satellite and approximate receiver position, x is the vector of unknown parameters, considered as the difference between the estimated and approximate values, and e is the random error vector, assumed as noise in the fault-free case with a zero mean. The RAIM algorithm has to be able to protect/warn the user against all possible anomalies that may affect the system. In this study, we adopt an approach similar to the MHSS of ARAIM method (Blanch et al. 2015). The different possible types of anomalies affecting the system will represent N_a alternative hypotheses $\mathcal{H}_k$, with $k = 1, \ldots, N_a$, where we assume:

$$\mathcal{H}_k : \quad y = Ax + \nabla y_k + e \tag{2}$$

where $\nabla y_k = C_k \nabla_k$ is the bias (due to an anomaly) affecting the observations, constituted by a matrix $C_k \in R^{m \times q}$, which defines the corresponding alternative hypothesis, i.e. the observations that are suspected to be faulty, and by an unknown bias vector $\nabla_k \in R^q$. q is the number of observations affected by the anomaly, for which it holds $1 \leq q \leq \mathrm{rd}$, where ($\mathrm{rd} = m - n$) is the degrees of freedom of the system, i.e. redundancy of the observations. Presence of a bias in one or more measurements can be due to satellite clock failures, ephemeris error, signal deformations, ionosphere disturbances, receiver malfunction or overheating, multipath etc.

After defining the multiple hypotheses that describe possible anomalies, one needs to make a prior assumption about the probability of occurrence of each hypothesis. Let us restrict our focus on anomalies that affect either a single observation per time or a limited number of observations. Typically, there is no need to test more than 2 simultaneous faulty satellites resulting from signal deformation, i.e. $q = 2$. However, in this initial study, the possibility of having 3 anomalous observations is additionally considered for those caused by undetected multipath or NLOS (by the NLOS detection method). Therefore, the protection level, discussed in the next section, provides an upperbound of the positioning error due to the errors that might be misdetected in this multiple hypothesis model.

2.2 Computation of the Protection Levels

The positioning integrity is often determined by computing the Protection Levels (PL), where integrity is considered available when the PLs are smaller than maximum allowed error upperbounds, defined by the Alert Limits (AL) (El-Mowafy & Yang 2016). AL is predefined according to the application requirements. Another important requirement that is also application-dependent is the continuity, i.e. the complement of the allowed probability that an alert will be issued during an operation or within a certain time interval, causing an interruption of the operation or positioning service disruption on the road. The continuity requirement translates into a requirement on the Probability of False Alarm (P_{FA}), which is the probability that an alert is raised when there is no fault; i.e. continuity = 1 - P_{FA}.

In this study, the PLs are computed based on the MHSS algorithm. Since we are generally not interested in the vertical component of the position in land navigation, we restrict our focus only on the Horizontal PLs (HPL). Furthermore, in land navigation, such as in pedestrian or vehicle navigation, positioning is better be expressed in terms of the along-track component and the cross-track component of the horizontal position. This allows us to distinguish between an along-track PL (denoted as $\mathrm{PL_{AT}}$) and a cross-track PL ($\mathrm{PL_{CT}}$).

The $\mathrm{PL_{AT}}$ and $\mathrm{PL_{CT}}$ at each epoch are the solutions of the following equations (Blanch et al. 2015):

$$\begin{aligned} 2\Psi\left(\frac{\mathrm{PL_{AT}}-b_{0,1}}{\sigma_{\hat{x}_{0,1}}}\right)+\sum_{k=1}^{N_a} p_k\Psi\left(\frac{\mathrm{PL_{AT}}-l_{k,1}-b_{k,1}}{\sigma_{\hat{x}_k,1}}\right) &= \zeta(P_{\mathrm{HMI}}-P_{\mathrm{un}}) \\ 2\Psi\left(\frac{\mathrm{PL_{CT}}-b_{0,2}}{\sigma_{\hat{x}_{0,2}}}\right)+\sum_{k=1}^{N_a} p_k\Psi\left(\frac{\mathrm{PL_{CT}}-l_{k,2}-b_{k,2}}{\sigma_{\hat{x}_k,2}}\right) &= (1-\zeta)(P_{\mathrm{HMI}}-P_{\mathrm{un}}) \end{aligned} \quad (3)$$

where Ψ denotes the tail probability of the cumulative distribution function of a zero-mean unit Gaussian distribution, assuming errors are normally distributed as mentioned earlier; P_{HMI} and P_{un} are the probability of Hazardous Misleading Information and that of the unmonitored observations. ζ is an arbitrary value between 0 and 1 used to weight the risk associated to the AT and CT directions, for instance in forward collision warning an initial arbitrary choice could be $P_{\mathrm{HMI}}^{\mathrm{AT}} > P_{\mathrm{HMI}}^{\mathrm{CT}}$.

Note that the second term in 3 is the sum of the product of two small values, p_k and $\Psi(..)$, and as such it is a very small value. The total number N_a of the tested alternative hypotheses depends on the scenario considered and number of the observed satellites. The p_k is computed based on the following:
- For each of the observed satellites, the prior probability of a single satellite fault P_{sat}, which is determined on the basis of expected system performance (the design requirements of the GNSS system) and the monitored performance over system life. In this work, we assume $P_{\mathrm{sat}} = 10^{-5}$/hour, for all observations from all GNSS systems. This value is suggested for GPS based on its Interface Control Document (e.g. ICD-GPS-200H). More research is currently underway to define P_{sat} for other constellations.
-The probability of multiple satellite faults, that is assuming two simultaneous faulty satellites, is taken as 1.3×10^{-8} (El-Mowafy & Kubo 2017). There is no need to consider more than two simultaneous faulty satellites as the probability will be insignificantly small (Blanch et al. 2015).
- It is assumed that the NLOS detection algorithm is able to take care of this type of anomalies, and what is left will have a low probability, assumed here as an arbitrary value of 0.001. This value is used for demonstration of the concept and will undergo further refinement in our future work. The presence of these faults in the satellites and NLOS is not an issue as long as they can be detected in the fault detection stage and when the remaining 'good' satellite observations enable positioning.

For illustration on how p_k and N_a are defined, let us consider a simple example where six satellites are observed. In the open sky scenario where NLOS is not considered, the total number of N_a for the multiple alternative hypothesis will include six possible single satellite faults, with p_k= P_{sat}, and 15 possible combinations of faults in two satellites simultaneously with p_k=1.3×10^{-8}. Thus, in the open-sky environment, N_a = 21. When considering the urban scenario, and assuming that NLOS affects a maximum of three satellites out of the six (e.g. the other three have high elevation angle, and utilizing the 3D model data), for the first case of single satellite faults, three satellites will have p_k= P_{sat} + 0.001, and three satellites will have p_k= P_{sat}. Likewise, in the case when considering dual-satellite faults, where in each of the 15 possibilities, for the satellites that are considered for NLOS, p_k=1.3×10^{-8} + 0.001, and the satellites that are assumed without NLOS will be assigned p_k=1.3×10^{-8}. Similarly, for the three-satellite case of NLOS, where 20 possibilities exist for the six satellite example. Thus, N_a will equal to 41 (i.e. 6 + 15 +20) in total.

The $b_{0,g}$ and $b_{k,g}$ ($g = 1$ for AT and $g = 2$ for CT) denote the biases on the along-track or cross-track direction under the considered null and alternative hypotheses, selected to bound maximum possible nominal biases in the range observations. Such biases are computed as follows:

$$\begin{aligned} b_{0,g} &= \sum_{j=1}^{n} |S^*(g,j)| \,.\, b_j \\ b_{k,g} &= \sum_{j=1}^{n} |S_k^*(g,j)| \,.\, b_j \end{aligned} \quad (4)$$

where $S^* = R\left(A^T Q_y^{-1} A + Q_{\hat{x}}^{-1}\right)^{-1}\left[A^T Q_y^{-1} \mid Q_{\hat{x}}^{-1}\right]$ is the projector from the observations domain to the unknowns domain, S_k^* is obtained with the same S^* formula substituting A by $[A \mid C_k]$ and b_j is the j-th component of the nominal bias vector b.

An overall horizontal circular HPL can be computed when the direction of motion is not precisely known or is changing fast (for instance, when undertaking a rapid turn), where:

$$\mathrm{HPL} = \sqrt{\mathrm{PL_{AT}}^2 + \mathrm{PL_{CT}}^2} \tag{5}$$

2.3 Fault Detection and Exclusion (FDE)

In ARAIM, the Solution Separation (SS) test statistics are computed as the difference between the position solutions under the different alternative hypotheses (tested possibilities of faulty satellite observations) and the null hypothesis. For each alternative hypothesis (k) considered, a difference vector ($\Delta\hat{x}_k$) is computed and a test is performed for each of the position components of the vector. The kth Solution Separation vector can be expressed as:

$$\underline{T}_{\mathrm{SS_k}} = \underline{\hat{\nabla}\hat{x}_k} = \underline{\hat{x}}_0 - \underline{\hat{x}}_k \tag{6}$$

where $\underline{\hat{x}}_0$ and $\underline{\hat{x}}_k$ are the position solutions obtained employing the null and the alternative model respectively,expressed as:

$$\begin{aligned} \underline{\hat{x}}_0 &= (A^T Q_y^{-1} A)^{-1} A^T Q_y^{-1} \underline{y} = S\underline{y} \\ \underline{\hat{x}}_k &= (A^T Q_{y_k}^{-1} A)^{-1} A^T Q_{y_k}^{-1} \underline{y} = S_k \underline{y} \end{aligned} \tag{7}$$

where $Q_{y_k}^{-1}$ is obtained from Q_y^{-1} replacing the diagonal elements corresponding to the faulty satellites in hypothesis $\mathcal{H}_k$ with 0 (this means giving a zero weight to such observations, and thus they are not considered). The test statistic is compared with a threshold $l_{k,g}$, which is set based on the availability requirement, and assuming that the statistic follows a normal distribution. The threshold can be expressed as:

$$l_{k,g} = K_{\mathrm{FA}} \sigma_{\hat{\nabla}\hat{x}_{k,g}} \quad \forall g = 1, 2 \tag{8}$$

Assuming equal allocation of the allowed P_{FA} between the along and cross-track directions gives:

$$K_{\mathrm{FA}} = \Psi^{-1}\left(\frac{P_{\mathrm{FA}}}{4N_a}\right) \tag{9}$$

where $\sigma_{\hat{\nabla}\hat{x}_{k,g}}$ is the standard deviation of the Solution Separation test statistic, which is obtained as the square root of the g-th diagonal element of the covariance matrix, such that:

$$Q_{\hat{\nabla}\hat{x}_k} = (S^* - S_k^*) Q_y (S^* - S_k^*)^T \tag{10}$$

If none of the statistics exceeds the threshold, the fault-free hypothesis is not rejected. If the test fails, the presence of faults is suspected and exclusion is attempted. A Chi-square (χ^2) test can also be applied

in the observation domain for confirmation of the FDE process. For more details about the FDE, the SS method and χ^2 test, the reader may refer to (Zhai et al. 2018) and (El-Mowafy 2019). In the event that the test continues to fail without identifying the faulty observations, an Alert is raised. When no faults are detected after applying the FDE, the PLs are re-computed and compared with the thresholds (AL). If $\mathrm{PL_{AT}}$ or $\mathrm{PL_{CT}} >$ AL, the solution is considered unavailable. On the other hand, when $\mathrm{PL_{AT}}$ and $\mathrm{PL_{CT}} <$ AL, the solution integrity is assumed available and the standard operations continue. Figure 1 illustrates a flowchart of the FDE process and integrity monitoring procedure using the SS method.

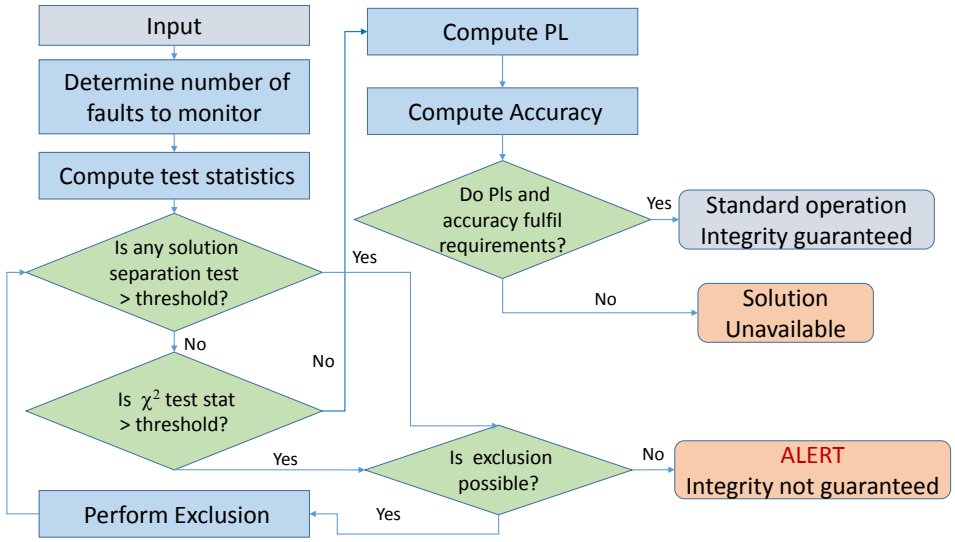

Figure 1: ARAIM baseline architecture. The algorithm checks the coherency of the observations by means of the Solution Separation tests.

3 Prediction of LOS, NLOS and multipath

A well-known challenge of urban GNSS positioning is the degraded GNSS signals. As shown in Figure 2, multipath is caused by multiple reception of signals from different transition paths due to the reflection by flat building s urfaces. The NLOS, however, occurs where the direct line-of-sight signal is blocked and only the reflected signal is received. Multipath effect can be reduced or mitigated by sophisticated antenna designs or narrow correlator-based discriminator designs (Zhdanov et al. 2002). However, these techniques have no significant improvement against the errors caused by NLOS. Many attempts have been made to detect and mitigate the effect of NLOS reception. For instance, Jiang & Groves (2014) utilize carrier-to-noise ratio measurements of dual-polarization to detect the NLOS, and (Groves & Jiang 2013, Hsu et al. 2017) applied consistency check methods. In recent years, 3D city models were rapidly developed to improve the performance of GNSS receivers in dense urban cities (Groves (2011)). Satellite visibility prediction can also benefit from the usage of 3D city models (Miura et al. 2015).

In this paper, the 3D city model is utilized to predict visible satellites at different locations along the user route and determine the occurrence of NLOS reception. The flowchart of the proposed method is shown in Figure 3. The modules mainly include 3D city model construction, estimation of user locations and GNSS ephemeris for prediction of LOS; GNSS measurements are then included when assessing the impact of multipath and NLOS during actual navigation. These modules are described in some detail in the following:

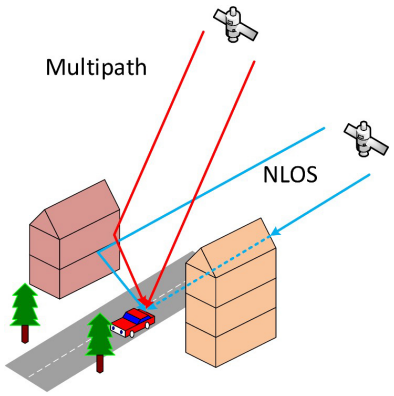

Figure 2: Multipath and NLOS effects.

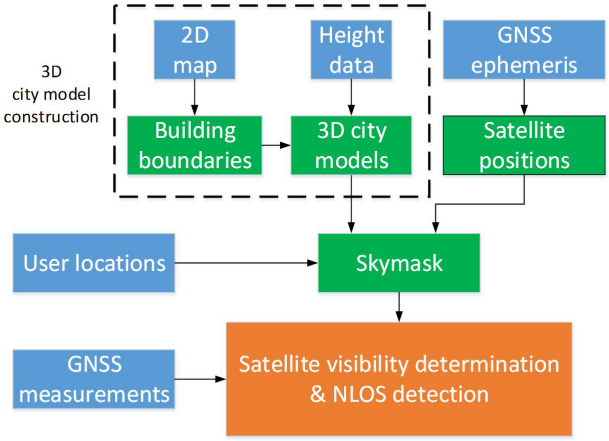

Figure 3: Satellite visibility determination and NLOS detection based on 3D city models.

3D city model construction: The 3D city model is established from a 2D map and the height data in Google Earth, which can be divided into three steps. First, the layouts and positions of the surrounding buildings on the map are obtained from the 2D map such as OpenStreetMap (OSM). Second, the coordinates of the building boundaries are extracted, forming a list of corner points of each building. Third, the boundary list is integrated with the height data to construct the level of detail 1 (LOD1) models. It should be noted that the 3D city model only contains the frame data of the building rather than the complex polygon data, thus reducing the storage size as well as the computation load for different usage. The presence of other objects, such as advertisement boards, that are large enough to obstruct the signal is in fact very low and thus was not considered. Figure 4a shows a typical urban area of Kowloon, Hong Kong, in Google Earth. The blue marker and the yellow line show the locations of the static and kinematic tests performed in this study, respectively, which will be discussed in the next section. Figure 4b shows the constructed 3D building model around the location of experiments. For real-time applications, the 3D city model construction can be pre-implemented to reduce the computational load.

User locations: User locations can be obtained using the conventional least squares method, or from prediction of the filtering result when enough number of satellites are observed. When multiple NLOS is expected, a particle filter is implemented to distribute position candidates (particles) around the receiver estimated position, which is assumed to be within about 15 m of the ground truth. For each candidate position, the proposed method can evaluate whether each satellite is in LOS, multipath or NLOS, by applying the ray-tracing procedure with a 3D building model (Hsu et al. 2015). According to the signal

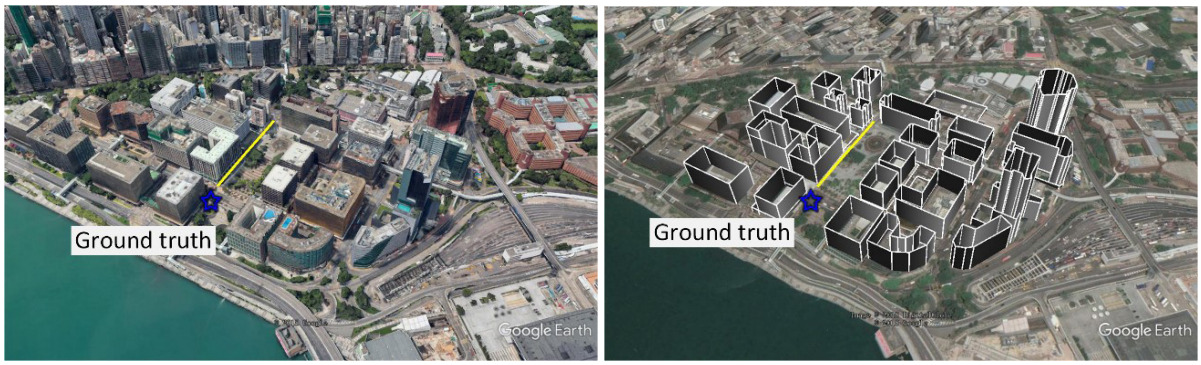

(a) 3D city model in Google Earth (b) Corresponding constructed 3D model

Figure 4: Constructed 3D city models.

strength, measured by the carrier to noise ratio (C/N0), the satellite could be roughly classified into LOS, NLOS and multipath scenarios. A simulated pseudorange of the satellite for the candidate position is next calculated. Ideally, if the position of a candidate is located at the true position, the simulated and measured pseudoranges should be identical. Therefore, the likelihood of each valid candidate is evaluated based on the difference between the measured and the simulated pseudorange by 3D building models and ray tracing. Finally, the expectation of all the candidates is the estimated position.

Computation of Satellite Positions: GNSS ephemeris are obtained from the decoded navigation message, providing the Keplerian orbit parameters of GNSS satellites. The calculation of satellite positions, azimuth and elevation angles can be found in Kaplan et al. (1996).

Estimation of LOS, NLOS: For the user locations, the building boundaries with the maximum elevation angle at each azimuth (from 0 to 360°) are plotted in polar coordinates, namely skymask (i.e. skyplot with building boundaries information), indicating the sky visibility. Figure 5a shows the skymask from the perspective of the static location in Figure 4. From geometry, and by comparing the elevation angle of each satellite with that of the building boundaries in the skymask at the same azimuth, satellite visibility can be determined. If a satellite angle is lower than that of the corresponding building boundary, it is classified as invisible, otherwise it is assumed v isible. It is straightforward that signals from satellites with lower elevation angles are more likely to be invisible. If a satellite is just within a tolerance area around the building boundary, which is set according to the 3D model accuracy and the expected precision of the estimated position, it is considered to be LOS. Figure 5b shows an example of the skymask with GNSS ephemeris information. The green and red indicate visibility and invisibility of the corresponding satellite, respectively. A NLOS is considered if a measurement is received from a satellite that is classified i nvisible. By excluding the NLOS measurements, the accuracy of the user position is expected to improve.

4 Testing

For demonstration of the proposed approach, and to show the benefit of combining ARAIM with NLOS detection method, testing is carried out in a static and kinematic experiments in an urban area in Hong Kong. Static data were collected for about half hour from UTC 12:20, 22th Jan 2018 using a u-blox M8T receiver, which outputs raw GNSS pseudorange measurements. Figure 6a shows the setup and location of the static test. Kinematic data was also collected on 4th April 2018 over a pedestrian walk of several

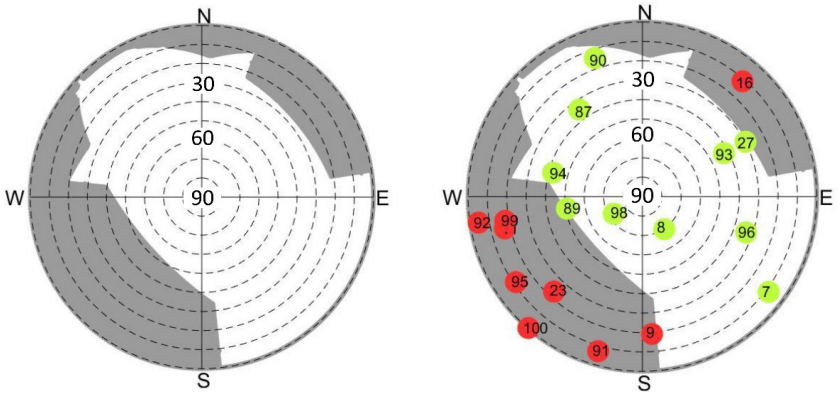

(a) Skymask based on 3D city model (b) Skymask with GNSS ephemeris

Figure 5: Example of skymask. PRN for GPS are between 1 and 32, for BDS are between 87 and 121.

minutes in the same urban area of the static test. The rover, equipped with a u-blox M8T receiver, moved on a straight line for a stretch of about 150 m, as shown in Figure 6b.

(a) Static test (b) Kinematic test

Figure 6: Experimental set-up and environments.

Figure 7 illustrates the skymasks at several selected representative epochs in the kinematic test. From the skymasks, the building boundaries vary over time. Hence, the visible satellites along the route are different, leading to a change in the LOS (observed satellites) and NLOS reception.

4.1 Static test results

Figure 8 shows the satellites in view during the static experiment, and the number of NLOS satellites individuated by the NLOS detection algorithm. Next, the results from processing in SPP and simulated DGNSS modes are discussed. Data from GPS and BeiDou (BDS) were used in the test. From Figure 8 we can see that in this static scenario the average satellite visibility for both GPS and BDS was 6 to 10 satellites in each constellation, giving a total satellite visibility of 12 to 19 satellites. The number of NLOS detected at each epoch in this urban environment was high, between 3 and 8 satellites.

For each scenario (SPP or DGNSS), the data was processed in four different modes:
i) without any augmentation,

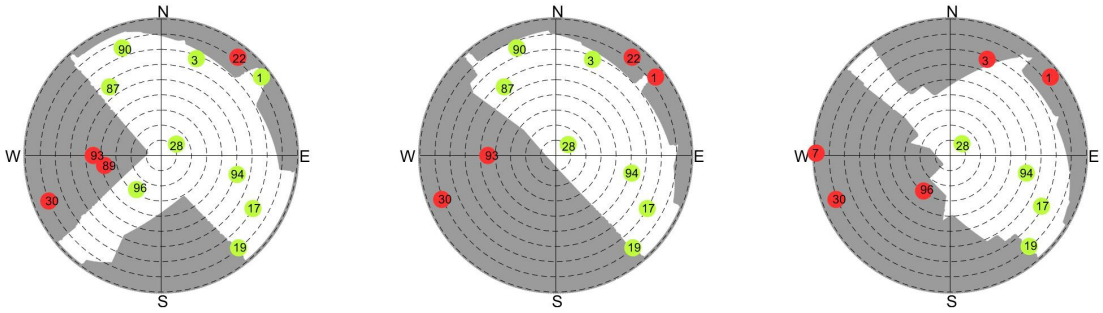

(a) epoch = 1s (b) epoch = 80s (c) epoch = 150s

Figure 7: Skymasks along the route at different epochs.

ii) with application of the NLOS detection algorithm,
iii) with application of the ARAIM algorithm, and
iv) with application of both NLOS detection and ARAIM algorithms.

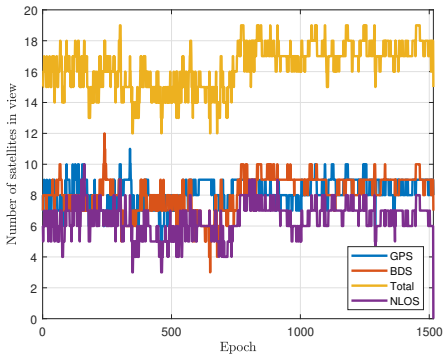

Figure 8: Number of satellites in view in the static test, and number of NLOS identified by the NLOS detection algorithm.

4.1.1 SPP static results

Figure 9 shows the horizontal positioning error, computed as the difference between the estimated and known positions, for the SPP case, with the subplots (a) no NLOS nor ARAIM algorithm implemented, (b) only the NLOS algorithm implemented, (c) only ARAIM algorithm implemented and (d) showing both NLOS and ARAIM algorithms implemented. The Horizontal Alert Limit (HAL) was set to 100m, the P_{HMI} is selected at 10^{-4}. Note that the used receiver in our tests was a commercial grade receiver and using SPP method, a large HAL would be expected. The main objective of this study, however, is to explore the benefit of combining ARAIM and NLOS detection as applied in urban environment, not necessarily in view of their adoption for the most demanding navigation safety applications. In this case, more precise GNSS techniques and receivers should be used, and this will be addressed in a future research. The error model used in ARAIM includes for the orbit and clock errors the User range error, URA/URE, which are extracted from the navigation message, and for the troposphere, mulitpath and user receiver error which are described in (Lee & McLaughlin 2007). The Klobuchar ionospheric

error model was used for the single-frequency receiver used. The multipath model used is designed for open sky environment, however, in the urban mode, multipath significantly varies according to the local environment, and thus is hard to model. This makes the implementation of the NLOS and multipath detection algorithm with ARAIM an attractive approach.

In our test, and for the cases in which ARAIM was applied (c and d in the figure), we distinguished between accepted positioning solutions and rejected solutions, i.e. for which the positioning service was declared unavailable (PL $>$ AL). Accepted positioning solutions are shown as blue crosses, and rejected solutions as brown circles. Positioning bias (mean error) and standard deviations reported in the figures are empirical estimates and were computed based on the accepted solutions only. The estimated bias and covariance ellipsoid are also shown, with a red line and a green ellipsoid, respectively.

We can notice that application of the NLOS detection algorithm only (case (b) compared to case (a)) does not result in an improvement of the positioning accuracy, instead the position solutions appear to aggregate into two clusters, one centered around the known position and the other instead shifted over 43m away in South-West direction due to undetected faults. However, when using both the NLOS detection and the ARAIM algorithms, comparing (d) with both (a) and (b), we notice an improvement of the positioning accuracy. This suggests that at most of the time, application of both algorithms correctly exclude erroneous observations. In particular, comparing case (d) with case (b), we can see that the cluster of position solutions shifted from the true position has been fully removed. The solutions accepted by the ARAIM algorithm have less position errors seen when comparing the standard deviation (σ) values between cases (a-b) and cases (c-d). Comparing case (c) with case (d), we can notice that the NLOS detection algorithm consistently improves the ARAIM performance, as both availability and accuracy significantly increased.

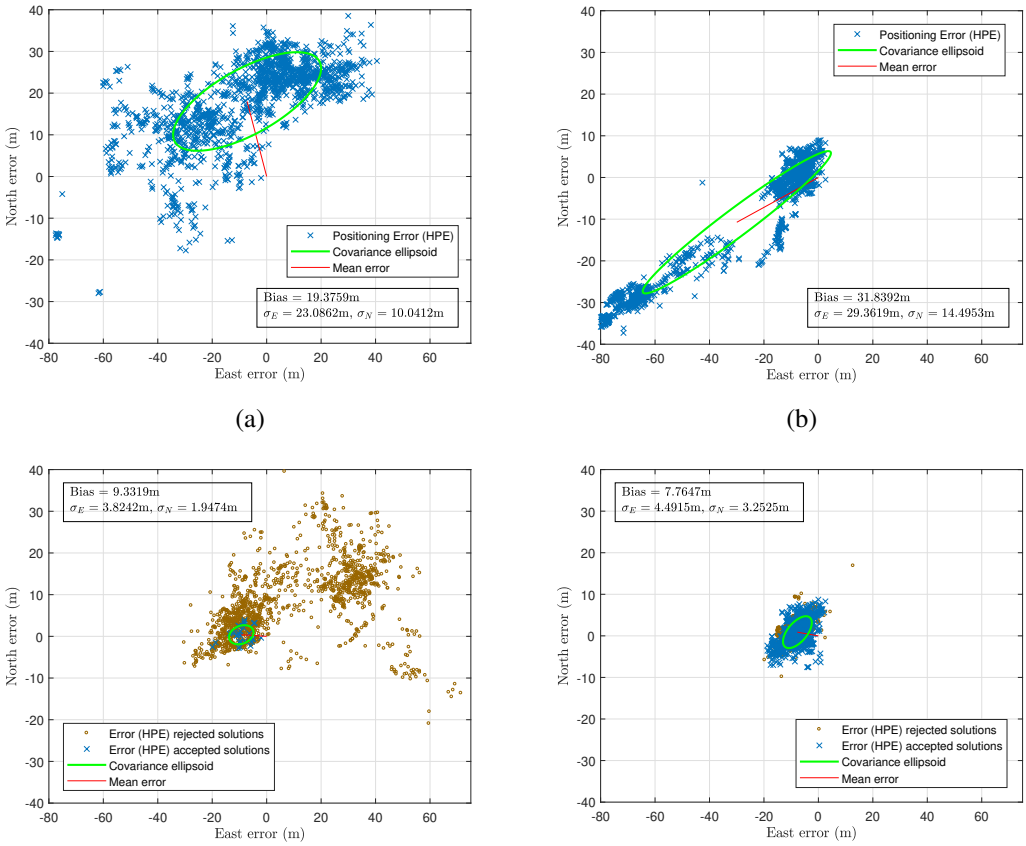

Figure 9: Horizontal position errors for the static test, SPP case: (a) no NLOS detection nor ARAIM, (b) NLOS detection implemented, (c) ARAIM implemented, (d) NLOS detection and ARAIM implemented. In cases (c) and (d) accepted solutions (blue crosses), and rejected solutions (brown circles). Empirical bias and stds are computed from accepted solutions only.

4.1.2 *Simulated DGNSS static results*

In this work, to simulate a DGNSS method, which is another method that may improve SPP results, we applied precise orbit and clock corrections, obtained from IGS products, to the observations. This method reduces the corresponding components of the measurements error, however, it does not address the atmospheric error and the hardware biases. The error model used in ARAIM was the same as the one discussed in the previous section for the SPP case, except for that standard deviations of the orbit and clock errors which were set as 5 cm and 0.1 ns, respectively, as suggested in (El-Mowafy et al. 2017). Figure 10 shows the results for the simulated DGNSS case. We can notice a strong similarity to the SPP case, and only small accuracy improvement and reduction of the size of the PLs. This is due to the fact that only orbit and clock corrections were applied, whereas positioning errors are dominated in this dense urban environment by observing a low number of satellites with poor geometry, presence of multipath and NLOS.

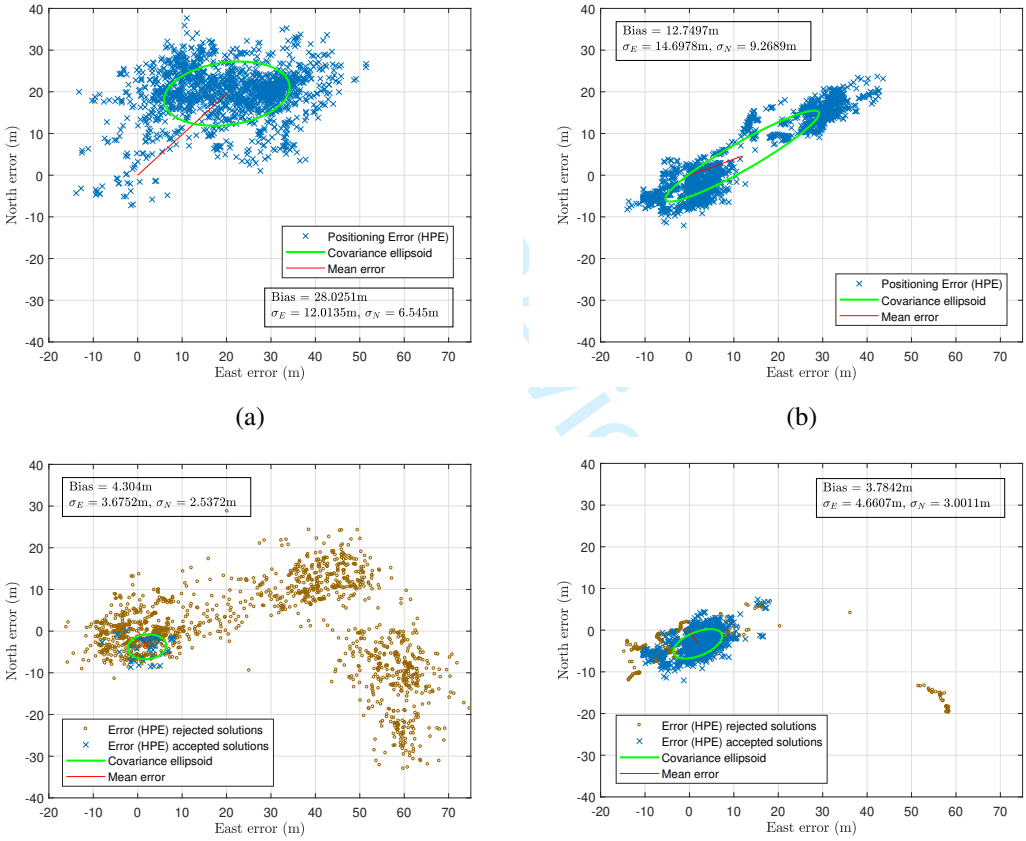

Figure 10: Horizontal position errors for the static test, simulated DGNSS processing case: (a) no NLOS detection nor ARAIM, (b) NLOS detection implemented, (c) ARAIM implemented, (d) NLOS detection and ARAIM implemented. In cases (c) and (d) accepted solutions (blue crosses), and rejected solutions (brown circles). Empirical bias and stds are computed from accepted solutions only.

Improvement of the positioning accuracy is again visible when both NLOS detection and ARAIM algorithms are used, comparing the subplot (d) with those of (a and b). Still a large number of Alerts is recorded after application of the ARAIM algorithm, in cases (c and d). The figure shows, however,

that the inclusion of NLOS detection reduces the rejected solutions with comparison to ARAIM only (d versus c). This indicates that the NLOS detection algorithm increases the coherency of the remaining observations as it successfully removed the observations responsible for the bias in positioning. However, the solutions accepted by the ARAIM algorithm are again characterised by a smaller positioning error. Therefore, the combination of the two methods is superior to the use of each one individually.

4.2 Kinematic test results

Figure 11 shows the satellites in view during the kinematic experiment, and the number of NLOS satellites. In the kinematic scenario, the satellite visibility was worse than that in the static scenario, with an average total number of satellites in view declining from about 14 at the beginning of the experiment to about 7 at the end. The number of NLOS on average was between 4 and 6 satellites (for GPS and BDS). The figure shows that due to signal obstruction, multipath and NLOS in this urban environment, availability is very low, and is concentrated in the first epochs, when a larger number of satellites was in view.

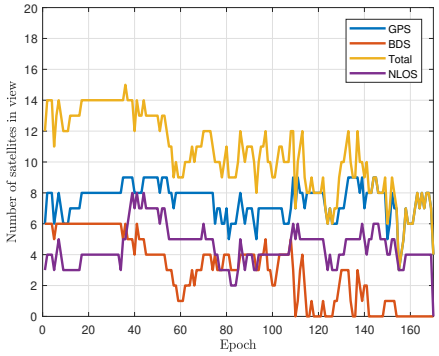

Figure 11: Number of satellites in view and number of NLOS in the kinematic test.

Figure 12 shows the horizontal positioning error when applying SPP, again for the 4 cases: (a) no NLOS nor ARAIM algorithm implemented, (b) only the NLOS algorithm implemented, (c) only ARAIM algorithm implemented and (d) both NLOS and ARAIM algorithms implemented. Accepted solutions are shown as blue crosses, and rejected solutions are shown as brown circles. For cases in which ARAIM was implemented, as stated before, the positioning bias (mean error) and the standard deviations are empirical estimates computed from the accepted solutions only. The estimated bias and covariance ellipsoid are also shown, with a red line and a green ellipsoid respectively.

Figure 13 illustrates the corresponding results for the simulated DGNSS case. We can notice a strong similarity to the SPP case, with only small accuracy improvement and reduction of PLs size. In both cases, SPP and DGNSS, and similar to the conclusions drawn in the static test, the NLOS detection algorithm application improves accuracy and reduces number of outliers, compared to the case with no NLOS detection algorithm nor ARAIM was applied (compare (b) with (a)). The application of the ARAIM algorithm again results in correct detection and exclusion of outliers, as from comparison of cases (c and d) with (a and b): accuracy of the accepted solutions is strongly increased, with biases and standard deviations are under 10m.

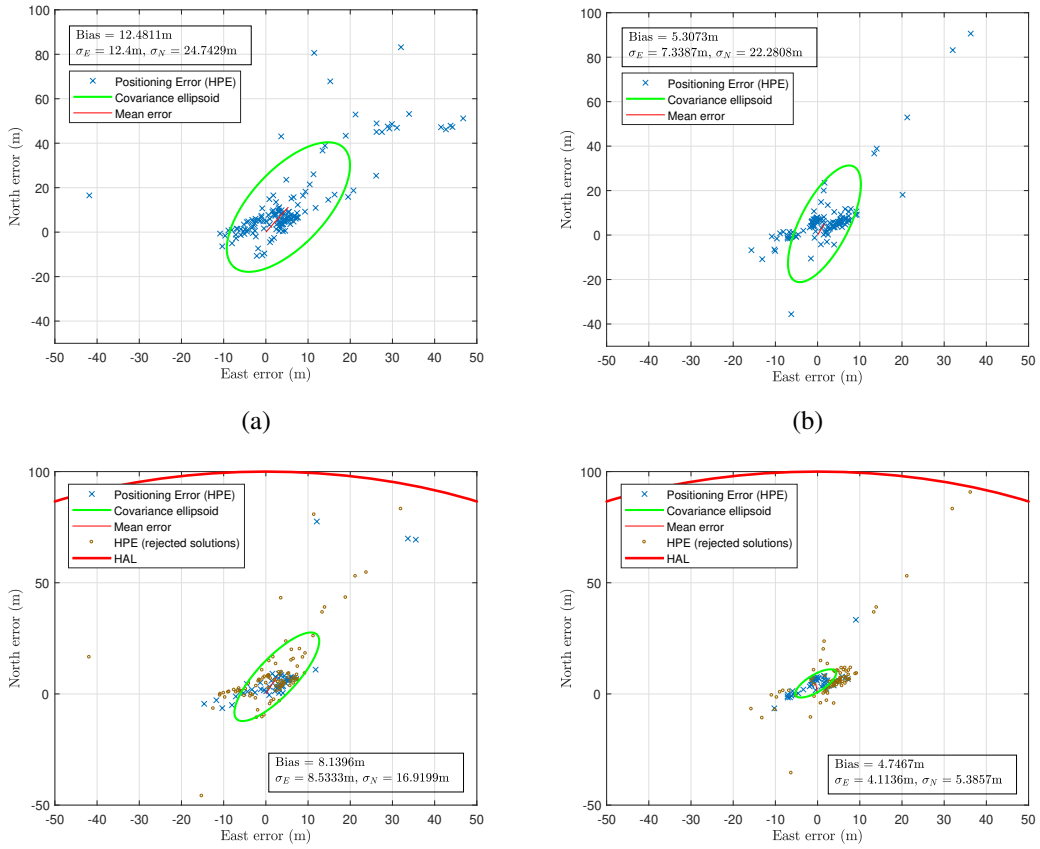

Figure 12: Horizontal position errors for kinematic test, SPP processing: (a) no NLOS detection nor ARAIM, (b) NLOS detection applied, (c) ARAIM implemented, (d) NLOS detection and ARAIM used. In cases (c) and (d) accepted solutions (blue crosses), and rejected solutions (brown circles). Empirical bias and standard deviations are computed from accepted solutions.

5 Discussion of the results

Table 1 summarizes the results of the different test runs. Positioning availability, mean error and standard deviations in the horizontal coordinates are reported for all the tests using SPP and DGNSS, and in the four modes considered, i.e. without NLOS nor ARAIM, with application of the NLOS detection algorithm only, with application of ARAIM only, and finally with application of both NLOS and ARAIM algorithms. Position availability was only assessed when applying ARAIM, i.e. for the cases of ARAIM only and ARAIM+NLOS. The position is considered available when PL $<$ AL using the observations passing the FDE test. IF PL $>$ AL, the position is considered unavailable.

Overall, in the urban environment, and based on test results we can conclude the following:

- The adoption of a NLOS algorithm complements ARAIM and improves its effectiveness, with a consistent increase of the positioning availability (e.g. in the static cases shown the positioning availability increased from less than 40% to more than 75%).

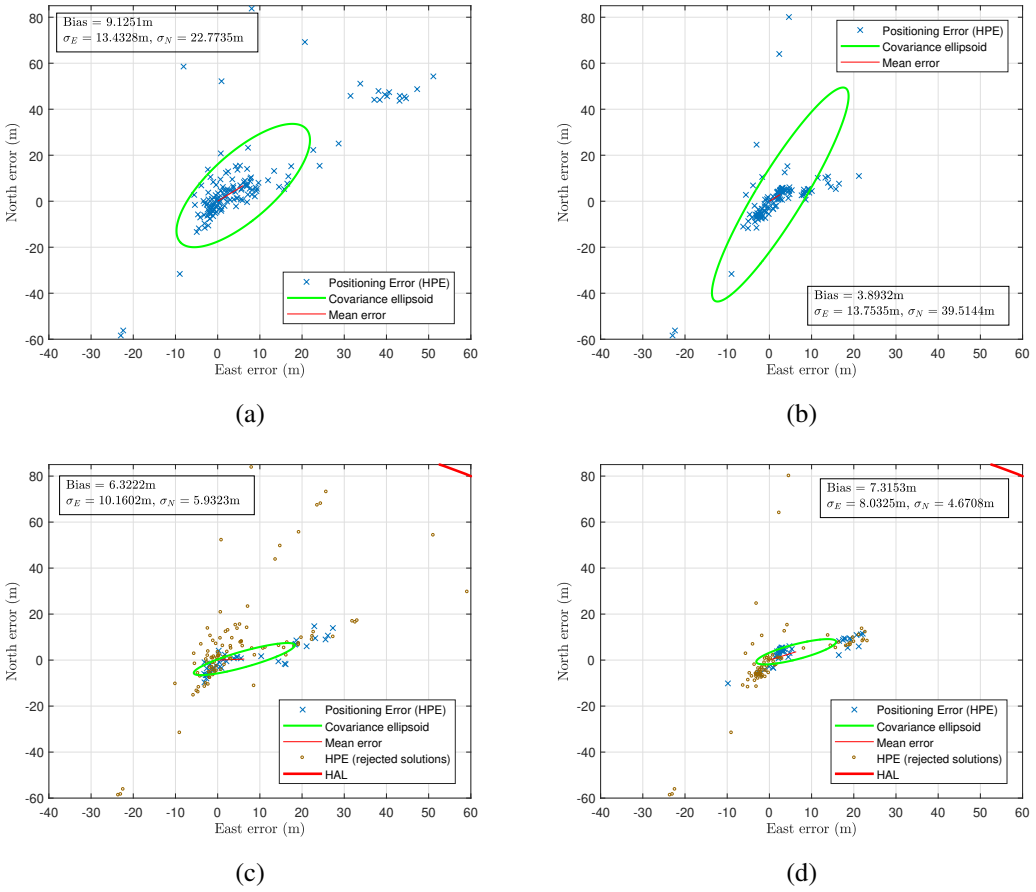

Figure 13: Horizontal position errors for kinematic test, DGNSS processing: (a) no NLOS detection nor ARAIM, (b) NLOS detection applied, (c) ARAIM implemented, (d) NLOS detection and ARAIM used. In cases (c) and (d) accepted solutions (blue crosses), and rejected solutions (brown circles). Empirical bias and standard deviations are computed from accepted solutions.

- In the urban environment, and due to reduced satellite number and geometry, even with a HAL value as large as 100m, the availability after implementing the ARAIM algorithm is low, i.e. $< 75\%$ for the static tests, and $< 37\%$ for the kinematic tests.
- Little difference in results is seen in this limited test between SPP and simulated DGNSS cases — this is due to the fact that the predominant sources of error in the scenarios under consideration are the limited number of observed satellites that also have poor geometry, NLOS and multipath.
- At present, the NLOS detection algorithm is time consuming, and can take a few seconds depending on the search region and speed of the user processor, which could vary widely. The ARAIM is not time consuming when applied properly. We expect in the future with possible improvements in the method and processing speed, the near real-time NLOS detection methods to be feasible. This will be addressed in our future work.

We can also see that both NLOS detection algorithm and ARAIM, while overall were effective in excluding erroneous and untrustworthy satellite measurements, suffered from the fact that too many observations were excluded from the processing in the urban environment, and the remaining positioning model became weak. A possible way to tackle this issues is to implement techniques that are able to

Table 1: Performance of the NLOS detection and ARAIM algorithms in terms of position availability, mean error and standard deviations of the accepted solutions.

Scenario			Availability %	Mean Error (m)	STD North (m)	STD East (m)
Static	SPP	No augmentation		1.49	10.1	23.1
		NLOS		31.8	14.5	29.4
		ARAIM	33	9.3	2.0	3.8
		NLOS+ARAIM	73	7.7	3.2	4.9
	DGNSS	No augmentation		28.0	6.5	12.0
		NLOS		12.7	9.3	14.7
		ARAIM	39	4.3	2.5	3.7
		NLOS+ARAIM	75	3.8	3.1	4.6
Kinematic	SPP	No augmentation		12.4	24.7	12.4
		NLOS		5.3	22.2	7.3
		ARAIM	30	8.1	16.9	8.5
		NLOS+ARAIM	34	4.7	5.3	4.1
	DGNSS	No augmentation		9.1	22.7	13.4
		NLOS		3.9	13.7	39.5
		ARAIM	31	6.3	5.9	10.1
		NLOS+ARAIM	37	7.3	4.6	8.0

make use of the measurement affected by NLOS or multipath, for instance, ray tracing algorithms (Hsu et al. (2016), Kumar & Petovello (2016)) and applying estimation techniques that de-weight suspect observations rather than excluding them.

6 Conclusions

In this contribution, a method is proposed that combines NLOS and multipath detection, based on the use of 3D-city models, with the ARAIM algorithm, when enough number of satellites is available to enable positioning with some redundancy. This is possible in large sections in the urban environment due to the use of multiple GNSS constellations. The first results of its application to SPP and DGNSS positioning in a static and a kinematic setups using a commercial-grade receiver have been demonstrated. Results show that NLOS detection and ARAIM complements each other, as results from the combined methods outperform the results from each algorithm alone, either in terms of accuracy of the position solutions, or in terms of availability of positioning. The NLOS detection algorithm is effective at individuating NLOS and multipath, as positioning accuracy improves after the exclusion of suspected NLOS observations, and the ARAIM algorithm is overall successful in determining the epochs in which the positioning is more trustworthy (i.e. improved integrity) and excluding biased observations. However, due to the challenging urban environment of the presented test and the use of a commercial-grade receiver, application of ARAIM resulted in low availability of positioning. The main issue with both NLOS detection algorithm and ARAIM, in the current implementation, is that the observations deemed untrustworthy are completely excluded from the solution, and the remaining positioning model may become weak, i.e. with limited observations to enable positioning. Improvement can be made by implementing techniques such

as ray tracing algorithms and integrity monitoring approaches that de-weight the observations affected by NLOS or multipath rather than excluding them, which will be addressed in our future work.

Acknowledgment

This study is supported by the Australian Research Council grant number DP170103341 to the first author. Davide Imparato helped in processing some of the data used.

References

Adjrad, M. & Groves, P. D. (2016), 'Enhancing least squares GNSS positioning with 3D mapping without accurate prior knowledge', *NAVIGATION* **64**(1), 75–91.

Blanch, J., Ene, A., Walter, T. & Enge, P. (2007), An optimized multiple hypothesis RAIM algorithm for vertical guidance, *in* 'Proceedings of ION GNSS 20th International Technical Meeting of the Satellite Division, Fort Worth Convention Center, Fort Worth, TX', pp. 2924–2933.

Blanch, J., Walter, T., Enge, P., Lee, Y., Pervan, B., Rippl, M., Spletter, A. & Kropp, V. (2015), 'Baseline advanced RAIM user algorithm and possible improvements', *IEEE Transactions on Aerospace and Electronic Systems* **51(1)**, 713–732.

Bourdeau, A. & Sahmoudi, M. (2012), Tight integration of GNSS and a 3D city model for robust positioning in urban canyons, *in* 'Proceedings of the ION GNSS 2012, Nashville, Tennessee', pp. 1263–1269.

El-Mowafy, A. (2019), 'On detection of observation faults in the observation and position domains for positioning of intelligent transport systems', *Journal of Geodesy* **93**(10), 2109–2122.

El-Mowafy, A., Deo, M. & Kubo, N. (2017), 'Maintaining real-time precise point positioning during outages of orbit and clock correction', *GPS Solutions* **21**(3), 937–947.

El-Mowafy, A. & Kubo, N. (2017), 'Advanced Receiver Autonomous Integrity Monitoring Using Triple Frequency Data with a Focus on Treatment of Biases', *Advances in Space Research* **59**(8), 2148–2157.

El-Mowafy, A. & Yang, C. (2016), 'Limited sensitivity analysis of araim availability for lpv-200 over australia using real data', *Advances in Space Research* **57(2)**, 659–670.

Groves, P. D. (2011), 'Shadow matching: A new gnss positioning technique for urban canyons', *The journal of Navigation* **64**(3), 417–430.

Groves, P. D. & Jiang, Z. (2013), 'Height aiding, c/n 0 weighting and consistency checking for gnss nlos and multipath mitigation in urban areas', *The Journal of Navigation* **66**(5), 653–669.

Hsu, L.-T., Gu, Y. & Kamijo, S. (2015), 'NLOS Correction/Esclusion for GNSS Measurement Using RAIM and City Building Models', *Sensors* **15**, 17329–17349.

Hsu, L.-T., Gu, Y. & Kamijo, S. (2016), '3D building model-based pedestrian positioning method using GPS/GLONASS/QZSS and its reliability calculation', *GPS Solutions* **20**(3), 413–428.

Hsu, L.-T., Tokura, H., Kubo, N., Gu, Y. & Kamijo, S. (2017), 'Multiple faulty GNSS measurement exclusion based on consistency check in urban canyons', *IEEE Sensors Journal* **17**(6), 1909–1917.

Jiang, Z. & Groves, P. D. (2014), 'Nlos gps signal detection using a dual-polarisation antenna', *GPS solutions* **18**(1), 15–26.

Joerger, M. & Pervan, B. (2016), 'Fault detection and exclusion using solution separation and chi-squared ARAIM', *IEEE Transactions on Aerospace and Electronic Systems* **52(2)**, 726–742.

Kaplan, E. D., Leva, J. L. & Pavloff, M. (1996), 'Fundamentals of satellite navigation', *Understanding GPS- Principles and applications(A 96-41027 11-17), Norwood, MA, Artech House, 1996,* pp. 15–57.

Kumar, R. & Petovello, M. G. (2016), Sensitivity analysis of 3d building model-assisted snapshot positioning, *in* 'Proceedings of the 29th International Technical Meeting of the Satellite Division of the Institute of Navigation (ION GNSS+ 2016), Portland, OR, USA', pp. 12–16.

Lee, Y. & McLaughlin, M. (2007), Feasibility analysis of raim to provide lpv 200 approaches with future gps, *in* 'Proceedings of ION GNSS-2007, Fort Worth, TX, 25-28 September 2007.', pp. 2898–2910.

Miura, S., Hsu, L.-T., Chen, F. & Kamijo, S. (2015), 'Gps error correction with pseudorange evaluation using three-dimensional maps', *IEEE Transactions on Intelligent Transportation Systems* **16**(6), 3104–3115.

Parkinson, B. W. & Axelrad, P. (1988), 'Autonomous GPS integrity monitoring using the pseudorange residual', *NAVIGATION* **35**(2), 255–274.

Suzuki, T. (2016), Integration of GNSS Positioning and 3D Map using Particle Filter, *in* 'Proceedings of the 29th International Technical Meeting of the ION Satellite Division, ION GNSS+ 2016, Portland, Oregon, September 12-16', pp. 1296–1304.

Walter, T. & Enge, P. (1995), 'Weighted RAIM for precision approach', *Proceedings of the ION GPS-95, Palm Springs, September 1995* pp. 1995–2004.

Zhai, Y., Joerger, M. & Pervan, B. (2018), 'Gps vulnerability to spoofing threats and a review of anti-spoofing techniques', *The Journal of Navigation* **71**(6), 1281–1298.

Zhdanov, A., Zhodzishsky, M., Veitsel, V. & Ashjaee, J. (2002), 'Evolution of multipath error reduction with signal processing', *GPS Solutions* **5**(3), 19–28.